

# The colour magnitude relation for galaxies in the Coma cluster.

A. I. Terlevich<sup>1</sup>, N. Caldwell<sup>2</sup>, R. G. Bower<sup>3</sup>.

<sup>1</sup>University of Birmingham, Edgbaston, Birmingham. B15 2TT.

<sup>2</sup>F.L. Whipple Observatory, Smithsonian Inst., PO box 97, Amado, Az 85645, USA.

<sup>3</sup>University of Durham, South Rd. Durham. DH1 3LE.

Accepted 6th June 2001

## ABSTRACT

We present a new photometric catalogue of the Coma galaxy cluster in the Johnson U- and V- bands. We cover an area of 3360arcmin<sup>2</sup> of sky, to a depth of  $V = 20$  mag in a 13 arcsec diameter aperture, and produce magnitudes for  $\sim 1400$  extended objects in metric apertures from 8.8 to 26arcsec diameters. The mean internal RMS scatter in the photometry is 0.014 mag in V, and 0.026 mag in U, for  $V_{13} < 17$  mag.

We place new limits on the levels of scatter in the colour–magnitude relation (CMR) in the Coma cluster, and investigate how the slope and scatter of the CMR depends on galaxy morphology, luminosity and position within the cluster. As expected, the lowest levels of scatter are found in the elliptical galaxies, while the late type galaxies have the highest numbers of galaxies bluewards of the CMR. We investigate whether the slope of the CMR is an artifact of colour gradients within galaxies and, show that it persists when the colours are measured within a diameter that scales with galaxy size. Looking at the environmental dependence of the CMR, we find a trend of systematically bluer galaxy colours with increasing projected radius from the center of the cluster. Surprisingly, this is accompanied by a *decreased* scatter of the CMR. We investigate whether this gradient could be due to dust in the cluster potential, however the reddening required would produce too large a scatter in the colours of the central galaxies. The gradient appears to be better reproduced by a gradient in the mean galactic ages with projected radius.

## 1 INTRODUCTION

The progressive reddening of the integrated colours of elliptical galaxies with increasing luminosity is known as the colour-magnitude relation (CMR) (Faber 1973; Visvanathan & Sandage 1977; Frogel et al. 1978; Persson et al. 1979; Bower, Lucey & Ellis 1992a,1992b [BLE92a,BLE92b]). Despite being a far simpler relation than the Fundamental Plane (Dressler et al. 1987; Djorgovski & Davis 1987; Bender et al. 1992; Saglia et al. 1993; Jorgensen et al. 1993; Pahre et al. 1995), it nonetheless has similarly small levels of scatter. Traditionally, the slope seen in the CMR has been attributed to a mass–metallicity sequence (Dressler 1984; Vader 1986), with the massive galaxies being more metal rich, and thus redder, than the less massive ones. This tendency can naturally be explained by a supernova–driven wind model (Larson 1974; Arimoto & Yoshii 1987), in which more massive galaxies can retain their supernova ejecta for longer than can smaller galaxies, thus being able to process a larger fraction of their gas before it is expelled from the galaxy. In hierarchical models of galaxy formation (e.g., Kauffmann & Charlot, 1998), the CMR can be reproduced because metals are expelled from low mass galaxies as part of the feed-back process. Studies of the CMR in high red-

shift clusters find a ridge-line slope comparable to that of the local clusters; furthermore, there is no sign of a change in the range of magnitude over which the CMR may be traced (Ellis et al. 1997; Stanford et al. 1998; Kodama & Arimoto 1997; Kodama 1997; Kodama et al. 1998). These studies all point towards the galaxies which make up the CMR in the cores of rich clusters being primarily constituted of uniformly old stellar populations. Given this metallicity driven interpretation of the CMR, its low levels of scatter in cluster cores implies that the galaxies are made up from uniformly old stellar populations (BLE92b; Bower, Kodama & Terlevich 1998). Even small variations in the ages of the galaxies would lead to unacceptable levels of scatter in young stellar populations, whereas old stellar populations have a much smaller age dependency in their colours.

Despite the uniformity of the CMR between the Coma and Virgo cluster cores (BLE92b), studies of the CMR in Hickson compact groups (Zepf et al. 1991) show increased scatter. Similarly, studies of field ellipticals (Larson et al. 1980) indicate that the scatter in the CMR could depend on environment. However these group and field galaxy samples contain data from many disparate sources, therefore there might be an added source of scatter from matching

the various photometric datasets onto a single photometric system. These additional sources of scatter can take the form of uncertainties in K-corrections for galaxies at different redshifts, or biases introduced due to sampling only the brighter end of the luminosity function at higher redshift in a magnitude limited sample. Despite this, at least in the sample of (Larson et al. 1980), the extra scatter seems too large to be accounted by increased observational uncertainties alone. Kodama et al. (1999) analysed the CMR in the Hubble Deep Field North. Again they found an increase in the CMR scatter, and a possible indication that the slope of the CMR is flatter at high redshift in the field environment.

Further evidence for an environmental dependence of the CMR comes from studies of spectral line indices. Broad-band colours are notoriously inefficient at separating the effects of age and metallicity on a stellar population, a degeneracy neatly summarised by Worthey (1994) in his ‘2/3’ law ( $\Delta[Fe/H] \sim \frac{2}{3}\Delta\log(t)$ ). This has led to studies of the stellar populations of early type galaxies in the cores of clusters using spectral line indices chosen to break this degeneracy and disentangle the effects of age and metallicity. Such studies (e.g. Mehlert et al. 1998; Kuntschner 1998; Kuntschner & Davies 1998) show that the CMR is driven by metallicity variations with galaxy luminosity, rather than age. A direct comparison of colours and line-index methods by Terlevich et al. (1999) showed that the two approaches have comparable sensitivity.

The key question then is to determine how the uniform CMR seen in cluster cores transforms into the less tight CMR of field galaxies. In order to investigate how the CMR varies across the Coma cluster, between different regions and between different galaxy morphological types, we have undertaken a survey of  $(U - V)$  colours covering almost one square degree of the Coma cluster. Although the colours of the galaxies in Coma have been studied before, both in a wide area (e.g. Dressler et al. (1980); Godwin et al. (1983) [GMP]) and with high precision U and V band CCD data (BLE92a), the present study is unmatched in area and sensitivity to variations in stellar populations. We chose to use the Johnson (Johnson & Morgan 1953) U and V filters because they straddle the 4000Å break in the spectra of galaxies at low redshift, and are thus very sensitive to the ages of the stellar populations. They are especially sensitive to recent bursts of star formation (e.g. Worthey 1994; Charlot & Silk 1994)

The present study extends the photometry of BLE92a to a complete galaxy sample covering approximately four times the area (still centered on the core), and reaches to fainter limiting magnitudes. The extra coverage and depth will enable us to obtain colours for the abnormal spectrum ‘E+A’ galaxies of Caldwell et al. (1993; 1996), many of which are to be found in the South West corner of the cluster around a group of galaxies dynamically associated with NGC4839 (Baier 1984; Escalera et al. 1992; Colless & Dunn 1996). Significant advances in detector technology since the work of BLE92a, allows us to use much larger CCDs with greater U-band sensitivity. In order to cover the required area, we took tiled images giving us continuous coverage of the cluster. In contrast, BLE92a targeted individual galaxies. Because of the continuous coverage, our sample of galaxies is more complete than that of BLE92a, including all of

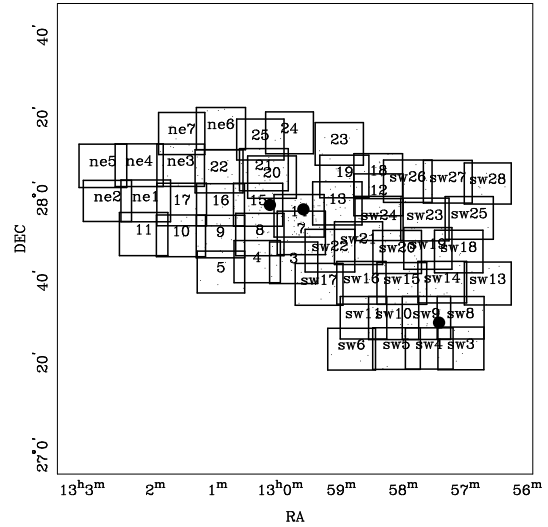


**Figure 1.** The distribution of observed images across Coma. All observed galaxies with  $V_{16} > 18$  are shown as a dot. The large dots show, from left to right, the positions of NGC4889, NGC4874 and NGC4839 respectively. The dynamical center of the Coma cluster is somewhere between NGC4889 and NGC4874, while the dynamical center of the substructure in the SW corner is NGC4839.

the GMP galaxies within our area of sky and with significantly higher precision than the GMP data.

## 2 OBSERVATIONS

The observing runs which provided data for use in this project are summarised in table 1. U and V-band observations were obtained in two successive years at the SAO 1.2m on Mt Hopkins, Arizona. The detector used was a thinned, back-side illuminated, AR coated  $2048 \times 2048$  Loral CCD in  $2 \times 2$  binning mode, giving us a 10 arcmin ( $192h^{-1}kpc$ ) field of view with 0.63 arcsecond pixels. The quantum efficiency of the CCD stays high and almost constant right across the U band, giving effective filter responses which approximate the standard shape. The same setup was used for all observations to maintain a common photometric system for the whole dataset. The average integration times used were 400s in the V-band and 45min in the U-band and the median V-band seeing achieved throughout the run was 2.2 arcsec FWHM (see appendix A).

The observations cover a continuous region encompassing the South West group around NGC4839, the central parts around NGC4874 and NGC4889 and also a large amount of the North East of the cluster (see figure 1). The observations were also designed to cover all of the Caldwell et al. (1993; 1996) abnormal spectra galaxies, however inclement weather meant that some were missed towards the extreme SW and NE. The presence of a seventh magnitude star just north of the center was also avoided as scattered light here makes data reduction difficult. To reduce any systematic differences in the photometry between parts of the cluster, observations of the central and SW regions were interleaved during the observing runs.

During the night, immediately after dusk and before twilight, standard stars from Landolt (1992) were observed

**Table 1.** Summary of observing time.

Dates	Observer(s)	Usable Nights
20–21 March, 1996	Caldwell	1.5
11–14 April, 1996	Caldwell & Terlevich	4
9–11 May, 1996	Caldwell	4
1–5 April, 1997	Caldwell & Terlevich	1.5

over a wide range in airmass. Care was taken to ensure the colours of the stars matched those of our galaxies, typically  $0 \leq (U - V) \leq 2$ . With our large field of view it was possible to observe many standards simultaneously. To have additional checks on the overall homogeneity of the final photometry, we used large overlaps of  $\sim 1$  arcmin between the actual Coma cluster images, ensuring that the objects in this overlap region were observed in both images. We also interleaved snapshots (300s and 100s for U and V respectively) of the central parts of the cluster, thus using the galaxies there as ‘standard’ galaxies. This is particularly important for the U band, as the spectral energy distribution of the standard stars is different from that of the early type galaxies.

### 3 DATA REDUCTION

The images were reduced using the standard methods in the IRAF package. The CCD used had a number of cosmetic defects, so in the subsequent reduction procedures, we mark objects within 5 pixels of a defect as suspect.

#### 3.1 Galaxy identification, photometry and astrometry

Lists of candidate objects were produced using the SExtractor1.2b10 program (Bertin & Arnouts 1996) from the V-band images. SExtractor was also used to differentiate the extended sources from the stellar sources in the images. All objects within 15 pixels (9.45arcsec) of a CCD edge were rejected. In order to avoid problems matching galaxies on the U-band frames, galaxies fainter than  $V = 20$  were not carried forward for further analysis. This gives rise to a sharp cutoff in the magnitude distribution of our catalogue.

The list of positions for the galaxies in each image was used by the IRAF `phot` package to generate fixed aperture magnitudes in 8.8arcsec – 30arcsec diameter apertures. The sky level was measured in annuli with inner radii of 50 arcsec. For the fixed photometric apertures with radii less than 20arcsec, we also measured the sky level at 25arcsec, and we give both values in the final data table. The magnitudes measured were then corrected for the varying seeing between the frames as described in Appendix 6. Astrometry for the frames was calculated using the HST guide star catalogue as a source of reference stars. The RMS scatter in our astrometry is approximately 1 arcsec. We have not corrected the data for geometric distortions in our detector, as they introduce photometric errors of less than 1% between galaxies at the centre and galaxies at the edge of the detector.

Observations of standard stars left residuals at the 0.03mag level in the U-band, once a drift in the zero point had been corrected. The drift (in all cases less than 0.2 mag per night) is also evident when examining the overlap regions

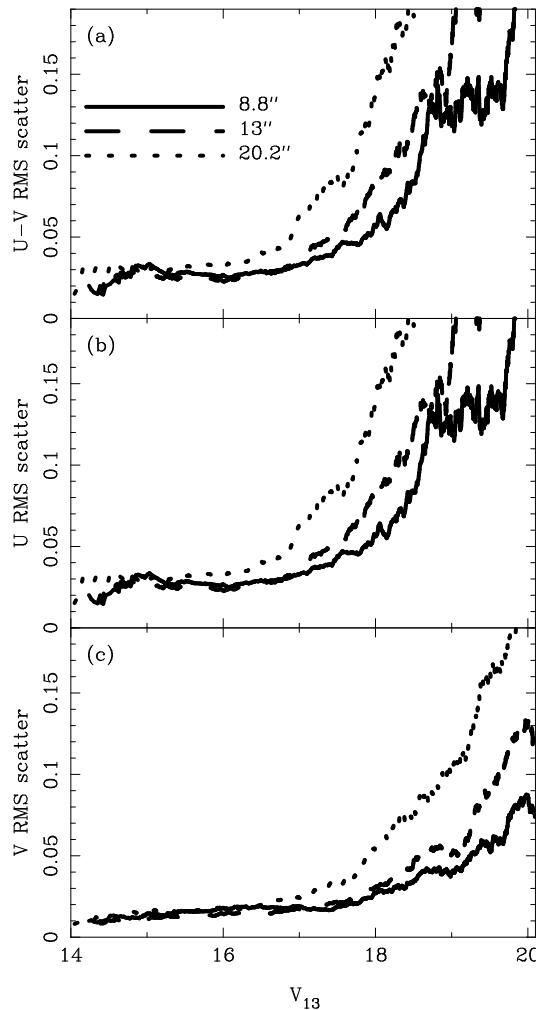


**Figure 2.** In the three panels, we plot the observational errors as a function of  $V_{13}$  magnitude, from repeated measurements of galaxies in overlapping regions. The  $(U - V)$  colour errors are shown in panel (a). Panels (b) and (c) show the errors for the U and V photometry. The three lines show a running bi-weight scatter (see section 3.2) measured through circular apertures of 8.8'', 13'' and 20.2'' diameter. A bin size of 60 observations was used in calculating the running mean, reducing to 6 at the bright extreme of the plot. Table 2 lists the mean RMS scatter down to  $V_{13} = 17$ mag for all of our apertures. The increasing levels of scatter with aperture size is entirely consistent with the increasing contribution of the sky to the noise with aperture radius.

between images and the repeated observations of ‘standard’ Coma fields. As these offsets were so readily measurable, we used them to improve the zero points of the individual images in order to ensure that the whole cluster is on a consistent photometric system for all the observations. The method we used to generate this system is very similar to that used by Maddox et al. (1990), and is described in detail in Appendix B. The absolute calibration of this system was set to agree with the published U and V band photometry of BLE92a.

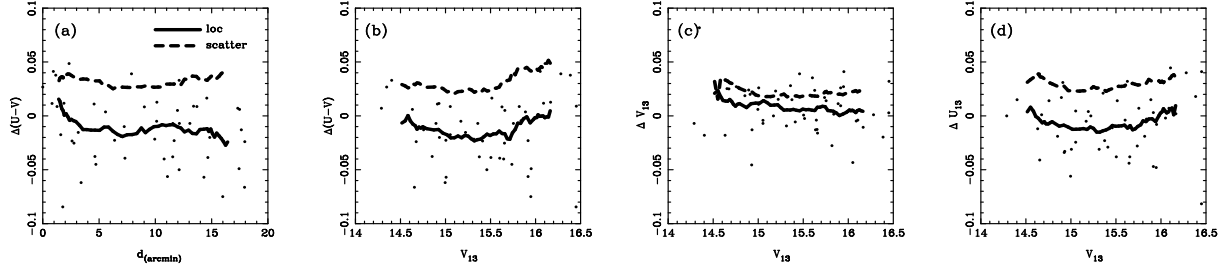


**Figure 3.** The four panels show the behaviour of the residuals between our 13arcsec diameter aperture photometry and that of BLE92a. In all cases, the residuals are calculated by subtracting the BLE92a data from ours, for example, a negative  $\Delta(U - V)$  indicates that our colour for a galaxy is bluer than the BLE92a colour. The Solid and dashed lines show running biweight location and scatter indicators. Panel (a) shows the difference between the  $(U - V)_{13}$  colours obtained in this paper and those of BLE92a, as a function of distance from NGC4874. Panel (b) shows how our colours compare to the BLE92a colours as a function of luminosity. Panels (c) and (d) show how our U and V band magnitudes compared with those of BLE92a.

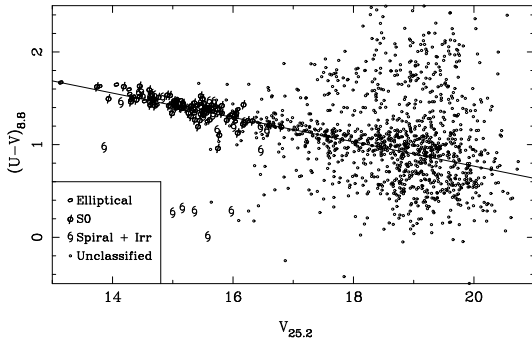


**Figure 4.** The  $(U, V)$  colour magnitude relation for all objects detected for which SExtractor gives a  $\text{CLASS\_STAR} \leq 0.2$ . The  $V$  are taken from the 25.2'' diameter aperture, as it is more complete than the 26'' aperture. In order to increase the signal to noise in the colour term, the  $(U - V)$  are taken from the smallest aperture, the 8.8'' diameter aperture. The symbols represent the morphological types of the galaxies from Andreon (1996; 1997). The small open symbols have no morphological information. The line is a biweight fit (see section 3.2) to the data, and follows the ridge-line of the CMR which can be seen to extend down to  $m_{V25.2} \sim 19.5$ .

**Table 2.** This table lists the RMS errors in our photometry for all of our apertures. It was generated using the repeated observations of both stars and galaxies, mostly in the regions of overlap between images. Figure 2 shows how the RMS errors vary with magnitude for the 8.8, 13 and 20.2 arcsec diameter apertures. The RMS internal scatter quoted by BLE92a for their 13'' photometry, which only reaches a magnitude of  $V_{13} = 16.5$  is 0.025 and 0.015 mag for U and V respectively.

Aperture diameter (arcsec)	RMS scatter		
	$U$	$V$	$(U - V)$
8.8	0.02303	0.01619	0.02829
12.6	0.02124	0.01364	0.02532
13	0.02258	0.01352	0.0264
16	0.0277	0.01478	0.03145
20.2	0.03036	0.01727	0.035
25.2	0.0359	0.02076	0.04154
26	0.04805	0.02706	0.05528

### 3.2 Quantifying the photometric errors

We can use the large number of multiply observed objects (mostly from the large overlaps between images) to constrain our observational errors. Table 2 lists the mean RMS scatter for all objects with  $V_{13} < 17$  mag in all of our apertures, and Figure 2 shows how the scatter in the observations of multiply observed objects increases with magnitude for the 8.8, 13 and 20.2arcsec diameter apertures. The scatter was computed using a running biweight scatter indicator (Beers et al. 1990). We use the biweight scatter indicator throughout this paper due to its robustness and resistance in the case of non Gaussian distributions. Additionally, we perform all regression analysis by minimising both the biweight scatter and location (mean) of the residuals to the fit. This provides an efficient way of performing fits to data which in the case of the CMR residuals, have a non Gaussian distribution, and often a large tail.

The levels of scatter in our 13arcsec apertures are the same as those quoted by BLE92a (0.025 and 0.015 mag for U and V respectively), and they stay constantly low down to  $V_{13} \sim 17$  mag. It should be noted that although table 2 shows that the 12.6'' aperture has the lowest RMS scatter in both U and V bands, figure 2 shows that fainter than  $V_{13} \sim 17$ , it is quickly overtaken by the 8.8'' aperture, which is better suited to the smaller sizes of the fainter galaxies.

As an independent check of our calibration, we have compared our photometry directly with that of BLE92a (see fig. 3). The scatter between our colours and theirs is 0.034 mag, while the scatter between our photometry and theirs is 0.022 and 0.032 mag for the V and U-bands respectively. This is almost exactly what we expect simply by adding the rms internal scatters of our data and theirs in quadrature. Equally important, given the method used to obtain a uniform photometric system for our data, is the fact that the mean colour difference does not vary as a function of distance from NGC4874 (figure 3, panel a).

### 3.3 The Photometric Diameter $D_V$

The photometric diameter parameter,  $D_V$  is equivalent to the  $D_n$  parameter used by Dressler et al. (1987), but is based on V-band photometry. We use the definition of  $D_V$  given in Lucey et al. (1991), viz.  $D_V$  is the photometric diameter (in arcsec) which encloses an area of average surface bright-

ness of  $19.80 \text{ mag arcsec}^{-2}$ . Like those of Lucey et al., our  $D_V$  include a  $(1+z)^4$  cosmological correction. As the  $D_V$  are (mostly) calculated using interpolation, they are very accurate. In order to measure  $D_V < 8.8 \text{ arcsec}$  (our smallest photometric aperture), we also need to perform some extrapolation, and we use  $D_V$ s only down to  $4 \text{ arcsec}$  to keep this to a stable minimum. The function we use for both interpolating and extrapolating is a simple  $R^{1/4}$  profile, which is fitted to the seeing corrected aperture magnitudes. In addition to rejecting  $D_V$ s smaller than  $4 \text{ arcsec}$ , we also do not attempt to calculate  $D_V$ s for galaxies where the function fit was poor, or where extrapolation of the data to larger radius is necessary. Comparison with the independent  $D_V$  values given by Lucey et al. (1991) for the same galaxies shows the uncertainty to be better than  $0.007 \text{ dex}$ .

### 3.4 Catalogue

An extract of the photometric catalogues are presented in Table 3. The full version, which is only available electronically, contains U and V-band photometry for all the apertures listed in table 2.

## 4 ANALYSIS TECHNIQUE

The first step in our analysis is to establish a criterion for cluster membership. Redshifts are available for all galaxies brighter than  $V_{13} = 15.7$ . For the fainter galaxies, 96% of galaxies with  $V_{13} < 16$ , 89% of  $V_{13} < 17$  galaxies, and 71% of  $V_{13} < 18$  galaxies have redshifts. The velocities were obtained from the NASA/IPAC Extragalactic Database\* (NED). Most of the velocities can be attributed to Colless & Dunn (1996). Galaxies with recessional velocities between  $4000 \text{ km s}^{-1}$  and  $10000 \text{ km s}^{-1}$  were taken as confirmed members of the Coma cluster. From this sample we then removed galaxies with ‘bad’ photometry. Galaxies were deemed bad, and thus rejected if

- Emission from a nearby object entered the  $13''$  diameter aperture.
- One of the CCD bad columns passes through the galaxy.
- A cosmic ray was removed from part of the galaxy in the V image (Cosmic rays in the U images were less of a problem due to the image being composed of multiple exposures).

The morphological classification of galaxies is taken from Andreon et al. (1996; 1997) which gives morphologies for all  $V_{13} < 15.7$  galaxies, but the morphologies don’t go as faint as the redshifts. 90% of  $V_{13} < 16$  galaxies, 68% of  $V_{13} < 17$  galaxies and 38% of  $V_{13} < 18$  galaxies have morphological information. The elliptical and late types are uniformly distributed throughout this magnitude range, however the proportion of S0 galaxies relative to the total number, has a sharp peak at  $V_{13} = 16 \text{ mag}$ , where 68% of the galaxies are S0s. The different symbols in figures 4, 6, 7 and 10 correspond to the broad morphological type of the galaxy.

\* The NASA/IPAC Extragalactic Database (NED) is operated by the Jet Propulsion Laboratory, California Institute of Technology, under contract with the National Aeronautics and Space Administration.

The actual morphological types used in these broad classifications are shown in table 4, together with the frequency of each type.

Regression analysis of the colour magnitude relation was performed using the biweight estimator. Our aim is to distinguish the ridgeline of the CMR, and we do not want to be unduly influenced by exact position of blue outliers. The biweight is a robust, resistant and efficient location and scale indicator, as is apparent from table 6. We compared the results of the biweight technique to that of using a biweight technique in conjunction with a  $3\sigma$  clipping of the dataset, however the difference was within the  $1\sigma$  error estimate of the un-clipped method.

The errors in the best fit relation were calculated by bootstrap resampling of the data. The observational uncertainties in the colour as a function of galaxy luminosity ( $O_c(L)$ ) are well known for this dataset (see fig. 2), so in order to make an estimate of how much of the measured scatter in the CMR is due to observational errors, we defined a mean observational colour scatter thus,

$$\bar{O}_c = \frac{\sum_{i=1}^N O_c(L_i)}{N}$$

where the  $L_i$  are the luminosities of the galaxies in the dataset, and  $N$  is the number of galaxies. Using this value for the observational errors, a value for the intrinsic scatter in the CMR can be calculated.

$$I = \sqrt{\sigma^2 - \bar{O}_c^2} \quad (1)$$

where  $\sigma$  is the observed scatter of the CMR.

Due to the fact that we are measuring the CMR scatter using a limited sampling of the underlying distribution, some uncertainty is introduced. This can make the measured scatter ( $\sigma$ ) smaller than the observational errors ( $\bar{O}_c$ ). In such a cases, we show the intrinsic scatter as zero, but we can still show an upper limit to the intrinsic scatter from the bootstrap limits.

## 5 ENVIRONMENTAL AND MORPHOLOGICAL VARIATIONS

Figure 4 shows the colour magnitude relation for every extended object in the photometric catalogue. Many of the objects shown will not be members of the Coma cluster, yet despite this, the CMR is clearly visible down to  $V_{25.2} = 19 \text{ mag}$ . We are interested in measuring changes in the CMR, such as in its scatter or slope, in different parts of the cluster, in different subsets of galaxy morphology, and for different luminosities. We therefore concentrate solely on those galaxies identified as members of the cluster from their recessional velocity. Using the recessional velocity avoids the need for statistical background subtraction. We have used the galaxies’ properties, such as morphology, luminosity and position, to define 14 subsets of these 275 member galaxies. The subsets are defined in table 5.

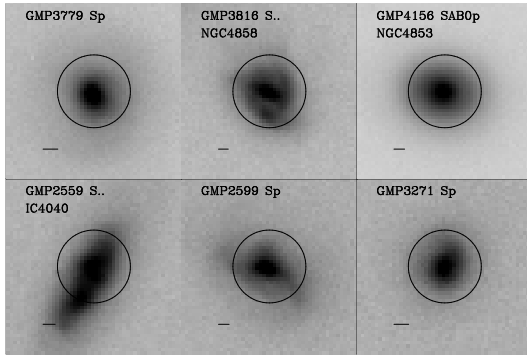
Figure 6 shows the CMR for all confirmed cluster members (dataset 1). The CMR is made up of galaxies of differing morphological types, and from every part of the cluster, yet it extends for almost five magnitudes without deviating from a straight line. Figure 4 shows that the CMR actually extends fainter than this in our data, but we have no redshifts

**Table 3.** A small extract of the photometric catalogue. Due to its size, The full catalogue is only available electronically.

GMP	RA J2000	DEC J2000	$\log_{10}(D_V)$	$V_{13}$	$U_{13}$	$V_{16}$	$U_{16}$
1807	13:01:50.2	27:53:36.2	0.943	15.322	16.727	15.161	16.570
1853	13:01:47.0	28:05:41.5	1.055	14.866	16.317	14.704	16.167
1885	13:01:44.1	28:12:51.4	0.628	16.747	17.957	16.630	17.845
2000	13:01:31.8	27:50:50.9	1.112	14.636	16.105	14.456	15.924
2048	13:01:27.2	27:59:56.8	0.821	16.039	17.435	15.938	17.338
2059	13:01:26.2	27:53:09.9	1.070	14.774	16.288	14.565	16.099

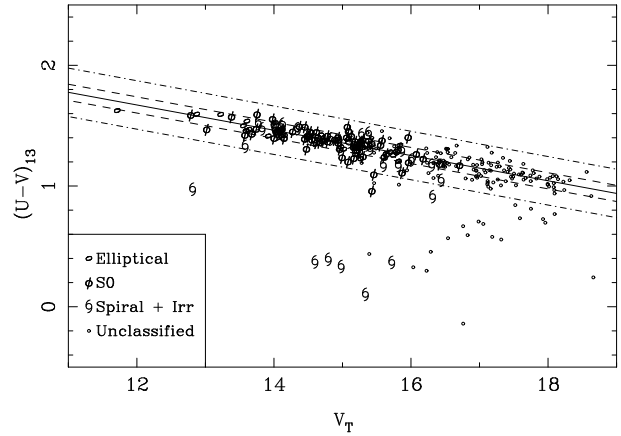
**Table 4.** The morphological classes used in this paper, combined into the broad categories of late-type, S0, and early type. Throughout the paper, no distinction shall be made between disk, boxy and undefined ellipticals (diE, boE, unE). They shall simply be referred to as ellipticals.

Category	Morphological type	Number of galaxies
late-type	Sp,S,SBa, Sa, SA0/a, SB0/a, SAB0/a, SAB0p	32
S0 type	SA0, SAB0, SB0, diE/SA0, diE/SAB0, unE/SA0	71
early type	Epec, boE, diE, unE	26
No morph		148

**Figure 5.** V band images of the late type galaxies which lie bluewards of the measured CMR for late type galaxies (dataset 7) by more than  $3\sigma$ . The four galaxies to the left of the plot are the four (out of a total of seven) Bothun & Dressler (1986) sample of blue disk galaxies in our surveyed environment. Out of these four, NGC4856 is the only galaxy not to have H $\alpha$  in emission. Bothun & Dressler conclude that these galaxies are undergoing a short burst of star formation activity. Additionally, NGC4853 is a post starburst galaxy identified by Caldwell et al. (1993), and is included here with the late types, as it has peculiar asymmetries in its light profile (Andreon et al. 1997). The circle in each figure represents the 13'' diameter aperture used in the measurements of both the colours and the magnitudes for the results in table 6. The line in the lower left of each panel shows the width of the seeing disk in each image.

for these faint galaxies. Secker et al. (1997) have shown that the  $(B, B - R)$  CMR in dwarf ellipticals in Coma, actually continues down to at least  $B \sim 21.5$ . Another important aspect of figure 6 is in the direction of scatter. There is almost no scatter red-ward of the CMR ridge line, even at the faint end where the observational errors are greatest, there is however significant blue-ward scatter, most of which is due to the late type population.

In the following sections, we investigate the properties of the CMR in each of the datasets (see figure 7. We use the techniques described in section 4 to ascertain the scatter about the main ridge line of the CMR, as well as the scatter

**Figure 6.** The colour magnitude relation for all galaxies with recession velocity within  $3000\text{km s}^{-1}$  of  $7000\text{km s}^{-1}$  (dataset 1). The magnitudes are estimated total V magnitudes ( $V_T$ ). Different colour symbols represent different morphological types as determined from Andreon et al. (1996; 1997). The solid line shows the best fit to the data using the biweight minimisation technique (see text). The solid line is a best fit to all the data points. The dashed lines show the  $1\sigma$  and  $3\sigma$  scatter.

in the total sample. Throughout the rest of the paper we use the 13arcsec diameter aperture magnitudes and colours (due to their low photometric errors) or colours measured within the  $D_V$  diameter (in order to define colours within an aperture that scales in galaxy size).

In order to verify whether the findings of the following sections can be attributed to variations in the CMR, rather than selection biases in the sample, we have investigated luminosity and morphological segregation within the samples. Using a K-S test, we find that the late-type and S0 samples have statistically indistinguishable luminosity distributions, but that the early type sample is on average 1mag brighter. We also find no correlation between luminosity and angular distance from NGC4874, nor any significant difference between the luminosity distribution of the E&S0 inner and E&S0 outer datasets (see figure 11).

**Table 5.** Selection criteria for each dataset. All datasets are a subset of dataset 1.

Dataset	Description
1	Confirmed members: After rejecting the ‘bad’ galaxies (see section 4), we classify all galaxies from $4000\text{km s}^{-1}$ to $10000\text{km s}^{-1}$ as members of the cluster. The velocities were obtained from the NASA/IPAC Extragalactic Database (NED). Most of the velocities can be attributed to Colless & Dunn (1996).
2	Confirmed members with $V_{13} < 17$ : A subsample of confirmed members (dataset 1) with the faint tail cut off at the point where the measurement errors in the colours starts to increase (see figure 2).
3	All with morphology: All member galaxies with a morphology from Andreon et al. (1996; 1997) (see table 4).
4	E&S0 morphology: All member galaxies with an elliptical or S0 morphological type (see table 4).
5	S0 morphology: All member galaxies with S0 morphology (see table 4).
6	Elliptical morphology: All member galaxies with Elliptical morphology (see table 4).
7	Late type morphologies: All member galaxies with late type (spiral and irregular) morphology (see table 4).
8	E&S0 center: Early type galaxies closer to NGC4874 than NGC4839.
9	E&S0 SW: Early type galaxies closer to NGC4839 than NGC4874.
10	E&S0 inner: Early type galaxies within $15'$ of either NGC4874 or NGC4839.
11	E&S0 outer: Early type galaxies further than $15'$ from both NGC4874 and NGC4839.
12	E&S0 bright: The bright half of dataset 4
13	E&S0 faint: The faint half of dataset 4
14	Members bright: The bright half of dataset 1
15	Members faint: The faint half of dataset 1

**Table 6.** Results of regression analysis on the  $13\text{arcsec}$  diameter aperture magnitudes. The errors quoted for the slope, intercept and observed scatter, are  $1\sigma$  bootstrap errors. The mean observational scatter ( $\bar{O}_c$ ) is used in calculating the intrinsic scatter (see main text).

Dataset	Number	Slope	Intercept	Observed scatter ( $\sigma$ )		$\bar{O}_c$	Intrinsic scatter ( $\sigma$ )			
				lower	upper		lower	upper		
(1) All members	275	$-0.128 \pm 0.001$	$3.37 \pm 0.1$	0.0744	0.0658	0.0835	0.029	0.069	0.059	0.078
(2) $V_{13} < 17$	175	$-0.139 \pm 0.003$	$3.55 \pm 0.2$	0.0674	0.0585	0.0751	0.025	0.063	0.053	0.071
(3) All with morph	129	$-0.142 \pm 0.003$	$3.59 \pm 0.2$	0.0599	0.0506	0.0675	0.024	0.055	0.044	0.063
(4) E&S0 morph	97	$-0.137 \pm 0.003$	$3.5 \pm 0.3$	0.0552	0.0471	0.0638	0.024	0.05	0.041	0.059
(5) S0 morph	71	$-0.125 \pm 0.007$	$3.32 \pm 0.4$	0.0583	0.0453	0.0683	0.023	0.053	0.039	0.064
(6) E morph	26	$-0.164 \pm 0.006$	$3.91 \pm 0.5$	0.0438	0.0298	0.0504	0.025	0.036	0.016	0.044
(7) Sp morph	32	$-0.166 \pm 0.01$	$3.96 \pm 0.7$	0.0778	0.0458	0.122	0.025	0.074	0.038	0.12
(8) E&S0 center	78	$-0.132 \pm 0.004$	$3.43 \pm 0.3$	0.0517	0.0435	0.0584	0.024	0.046	0.036	0.053
(9) E&S0 SW	19	$-0.15 \pm 0.009$	$3.71 \pm 2$	0.0735	0.0085	0.119	0.024	0.069	0	0.12
(10) E&S0 inner	55	$-0.149 \pm 0.005$	$3.71 \pm 0.3$	0.0542	0.0432	0.0636	0.024	0.049	0.036	0.059
(11) E&S0 outer	42	$-0.124 \pm 0.003$	$3.28 \pm 0.3$	0.0412	0.0282	0.0532	0.024	0.033	0.014	0.047
(12) E&S0 bright	49	$-0.135 \pm 0.007$	$3.49 \pm 0.6$	0.0461	0.0366	0.0528	0.025	0.039	0.027	0.046
(13) E&S0 faint	49	$-0.135 \pm 0.009$	$3.48 \pm 0.7$	0.065	0.049	0.081	0.023	0.061	0.043	0.078
(14) members bright	140	$-0.141 \pm 0.005$	$3.57 \pm 0.3$	0.0657	0.0557	0.075	0.024	0.061	0.05	0.071
(15) members faint	136	$-0.123 \pm 0.004$	$3.29 \pm 0.3$	0.086	0.069	0.107	0.054	0.067	0.043	0.093

### 5.1 Morphological dependence of the CMR

In this section we examine variations in the CMR of galaxies of different morphological types. We use the broad morphological types defined in table 4. The dividing lines between the various types is somewhat arbitrary, and we err towards the later morphological types, i.e. we classify a galaxy of type E/SA0 as S0, and one of type SA0/a as late type. We investigate the scatter of the main ridge line of the CMR, and the amount of blue-ward scattering separately. Initially we concentrate on the ridge line. Looking at the morphologically segregated datasets (3,4,5,6 and 7) in table 6, they all have levels of intrinsic scatter indistinguishable within the measurement errors ( $\sim 0.05$  mag), except for the elliptical galaxies (dataset 6) which has significantly lower levels of scatter ( $0.036\text{mag}$ ).

The only exception is the late type galaxy dataset (7): however, even this data set includes many objects that lie on the CMR ridge line. Six of the late type galaxies are very blue compared to the CMR ridge-line. The presence of these blue galaxies is not surprising. Figure 5 shows snapshots of the V band images of these galaxies, which even with our poor spatial resolution can be made out to be very obviously late type. The only S0 galaxy amongst these, NGC4853, was identified by Caldwell et al. (1993) as a post-starburst galaxy, and is included here with the late types due to peculiar asymmetries in its light profile. Perhaps the most surprising aspect of these blue galaxies, is not their presence, but the fact that there are only seven of them, out of the 32 late types in our sample. If we apply a  $3\sigma$  clipping to this data set, we obtain a CMR ridge-line that is indistinguishable from the S0 types. Figure 8 shows snapshots of the

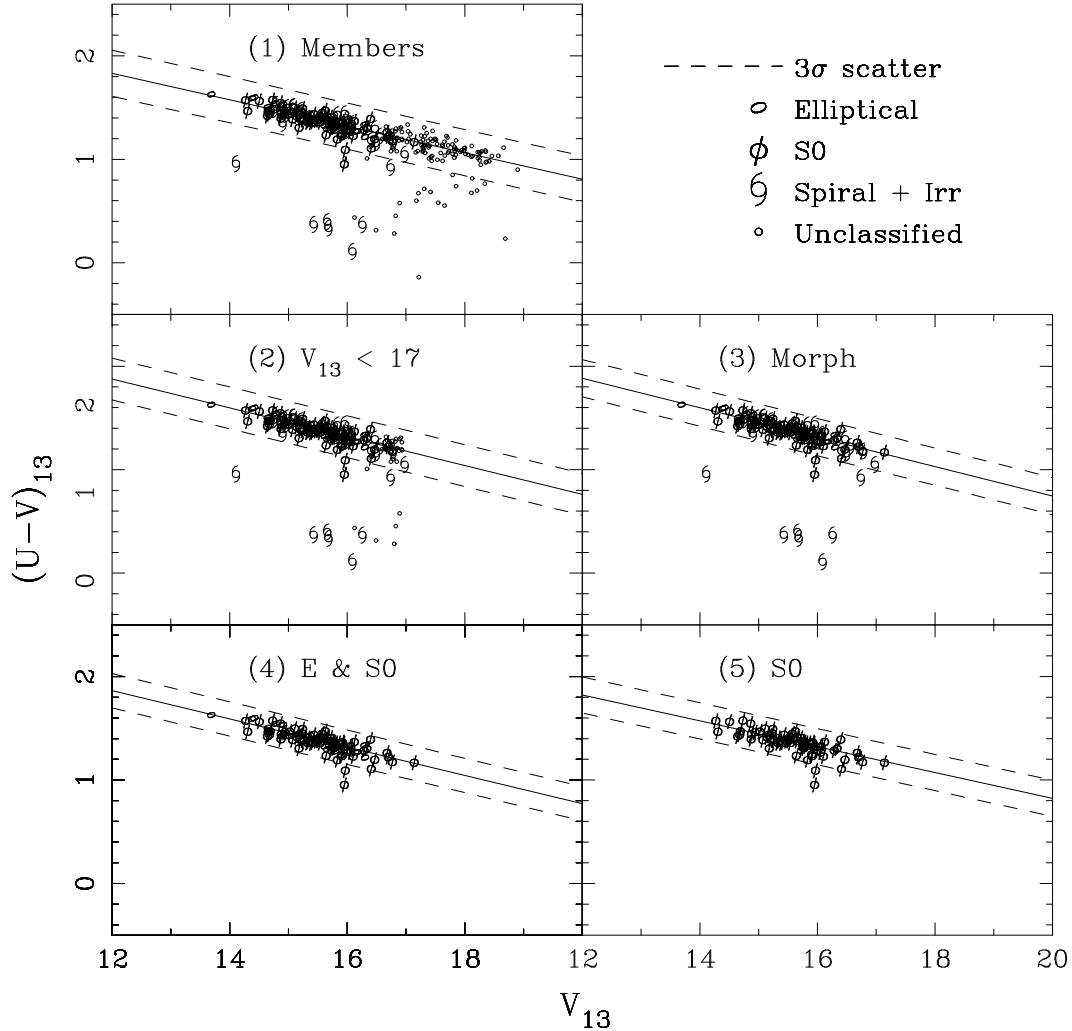


**Figure 7.** This figure (continued on pages 9 and 10) shows the CMRs for each of the datasets defined in the main text. The symbols are the same as those used in figure 6. Dashed lines represent the  $3\sigma$  scatter of the galaxies about the best fit line for the full dataset.

V band images of these ‘red’ late types. All of the galaxies in figure 8 are within  $3\sigma$  of the best fit CMR for dataset 6. Some of the galaxies are borderline SA0/a, however they are the minority, and cannot in themselves explain the low scatter. All of the ‘red’ late type galaxies appear to have fainter disks compared to the ‘blue’ ones in figure 5, however statistical tests show no correlation between a galaxy’s  $D_v$  and its CMR residual ( $(U - V) - (mV + c)$ , where  $m$  and  $c$  are the best fit slope and intercept for the CMR). There is however a strong correlation between CMR residual and colour gradient, and whereas the majority of galaxies have colour gradients in the sense that they get bluer with increasing radius, the blue galaxies have a colour gradient in the opposite direction (they get redder with increasing radius). Thus, although the ‘blue’ galaxies are not necessarily more compact (c.f. Moss & Whittle, 2000), the ‘blue’ light is more concentrated than the CMR galaxies. We conclude that the ‘red’ late types are ‘anemic’ (e.g. Van Den Bergh, 1991), i.e. that they have lost their *HI* gas through interactions with the intra cluster medium.

The only other dataset with large numbers of ‘blue’ galaxies, is dataset 1 (all cluster members). These blue

galaxies are, in addition to the late type galaxies noted above, morphologically untyped. Figure 9 shows V band images of all of the galaxies which deviate from the CMR ridge line for dataset 1 by more than  $5\sigma$ . It is immediately obvious that they are predominantly of late type (e.g. GMP4570), although in some cases it is difficult to tell (e.g. GMP3848).

## 5.2 Luminosity dependence of CMR

The last set of datasets are the ones where we segregated the galaxies according to their luminosity (12,13,14 and 15). We have separated the early type galaxies dataset (4) into two halves of equal numbers, with the bright half of the galaxies in dataset 12, and the faint half in dataset 13. Because dataset 1 spans a much larger range in luminosity than do the datasets with only morphologically typed galaxies, we split that into two halves too (datasets 14 and 15).

The bright and faint early type galaxies have indistinguishable slope and intercept, however the faint sample has greater intrinsic scatter. This could be related to the increasing numbers of blue galaxies at fainter magnitudes. As these

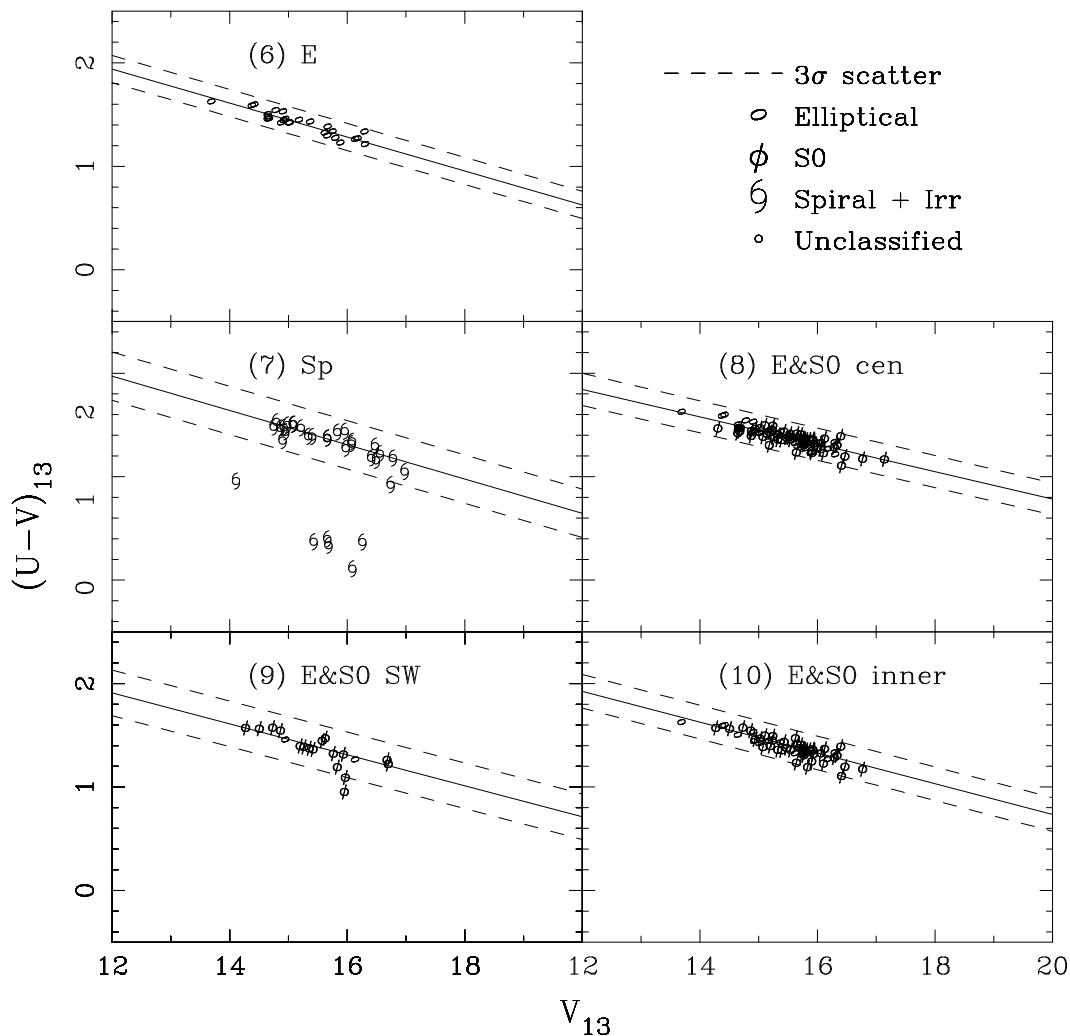


Figure 7 – continued

galaxies start to become apparent after  $V_{13} > 16$ , they are mainly untyped in our study.

The two halves of the complete members dataset, have differing slopes. It is possible that this could simply be due to aperture effects, but as we don't have reliable  $D_V$  measurements for the faint half of the dataset, we cannot check this directly (see below). Although the observed scatter in the faint sample is larger than that of the bright sample, it has twice the mean observational error ( $\bar{O}_c$ ). Once the difference in the observational errors is taken into account, both the bright and the faint samples have similar values for the intrinsic scatter.

A common concern over the interpretation of the CMR as a constraint on galaxy formation (eg., Kauffmann & Charlot, 1998; Bower et al., 1998) is that the role played by colour gradients within galaxies. Is it possible, for example, that the slope of the CMR is due to the metric aperture measuring a larger fraction of the total light in small galaxies than in larger ones? To address this effect, we have measured the colour within the  $D_V$  diameter of each galaxy. This gives a measure of the colour of each galaxy that scales with the properties of the galaxy. This approach is preferable to measuring the colour within a fixed fraction of the total light

**Table 7.** Results of regression analysis on the aperture magnitudes measured within  $D_V$  diameter apertures. For a complete description of each dataset see the main text. The errors quoted for the slope are  $1\sigma$  bootstrap errors.

Dataset	Number	Slope
(3) All with morph	111	$-0.0754 \pm 0.005$
(4) E&S0 morph	86	$-0.0819 \pm 0.004$
(5) S0 morph	63	$-0.082 \pm 0.006$
(6) E morph	23	$-0.0911 \pm 0.003$

since  $D_V$  is (usually) a radius at which the colour can be accurately defined and does not require extrapolation. In contrast, measurements based on the effective radius,  $R_e$ , require extrapolation of the radial profile, and often require the colour to be measured at a radius where the signal to noise ratio is low.

The colour-magnitude relation measured within  $D_V$  is shown in Figure 10. The slope of this relation is weaker than that measured within the fixed diameter, it is still clearly evident. Table 7 shows the slope of the relation for the whole sample and for the early-type data sets. Bower et al. (1998) estimated that the approximately 1/3 of the CMR slope was

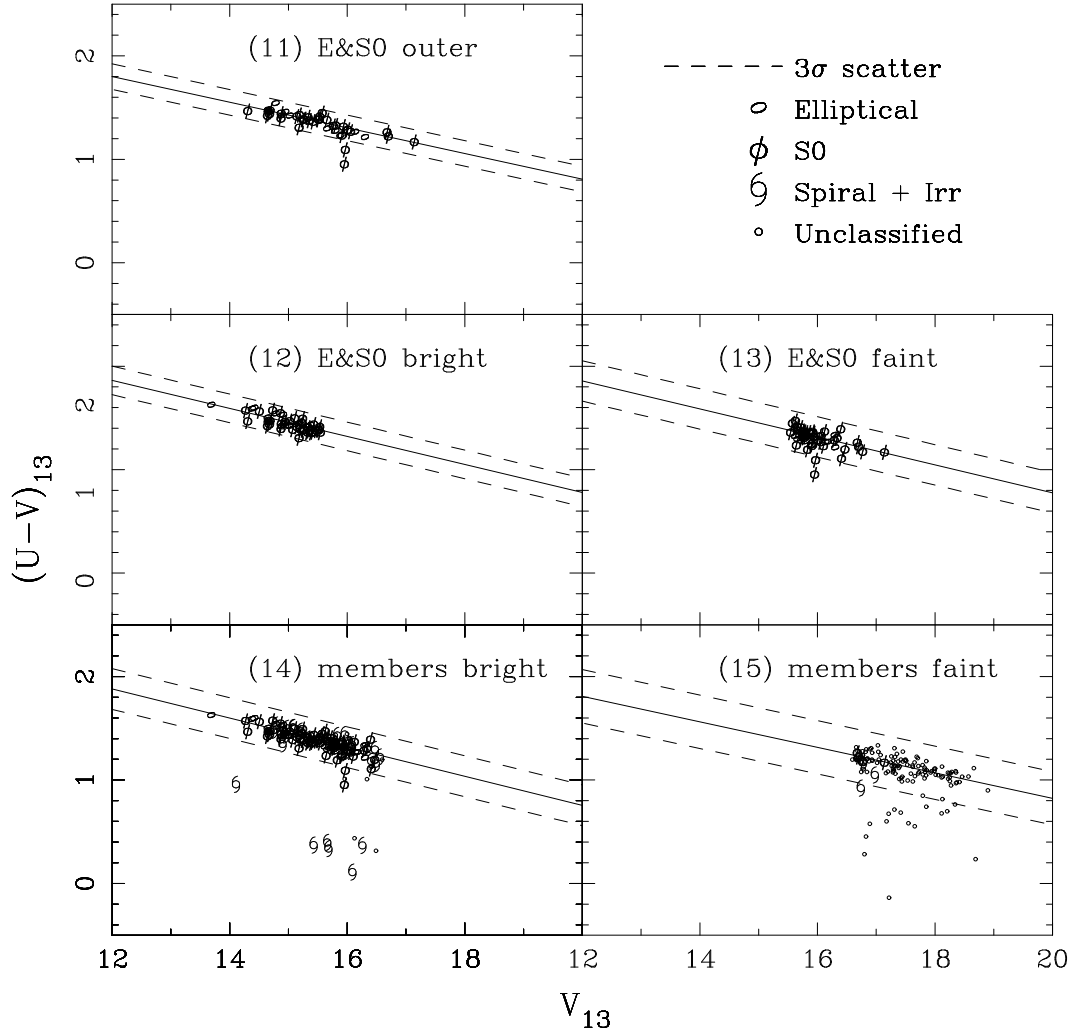


Figure 7 – continued

due to aperture effects. Comparison with Table 6 shows that the reduction in the slope is consistent with this. This dataset therefore confirms that the existence of the CMR slope is not an artifact due to radial colour gradients in the galaxies. Any model of cluster galaxy formation must therefore be able to simultaneously explain the small scatter of the relation and its slope. Importantly, this constrains the factor by which the masses of cluster galaxies can grow through random collisions between objects of different colours (see Bower et al. (1998) for a fuller discussion).

### 5.3 Environmental dependence of the CMR

In order to investigate the environmental dependence of the CMR, we have defined subsamples of the cluster members according to their position in the sky. Datasets 10 and 11 contain galaxies which are closer and further than 15arcmin of NGC4874 respectively, while datasets 8 and 9 contain galaxies which are either nearer to NGC4874 or NGC4839 respectively (see table 5). We have restricted ourselves to early type galaxies (ellipticals and S0s) to avoid as much as possible any bias arising from the morphology–density relation within the cluster, although section 5.1 showed there

to be little variation in the properties of the CMR ridge-line between the different morphological types.

#### 5.3.1 Significance of the environmental change

The low number of galaxies in the SW sample make it very difficult to measure its scatter, the measured scatter in the full dataset is  $0.07 \pm 0.06$ , so we instead concentrate on the scatter in the central and outer samples (datasets 10 and 11). Here we see something unexpected. The outer dataset has less scatter (both observed and intrinsic) than the inner dataset. Although it is only marginally significant, it is just the opposite of what we would expect. Figure 7 (panels 10 and 11) show the CMRs for these datasets. From them we can see that they both have similar numbers of elliptical and S0 galaxies. There are too few elliptical galaxies in each dataset to be able to measure the scatter reliably for just the ellipticals in each one, but it is possible for the S0 galaxies. This shows the effect to be unrelated to morphology, with the 41 inner S0 galaxies having an observed scatter of  $0.0597 \pm 0.02$  and the 30 outer galaxies having an observed scatter of  $0.0377 \pm 0.01$ . Figure 11 shows the luminosity distribution for both datasets, which are statistically

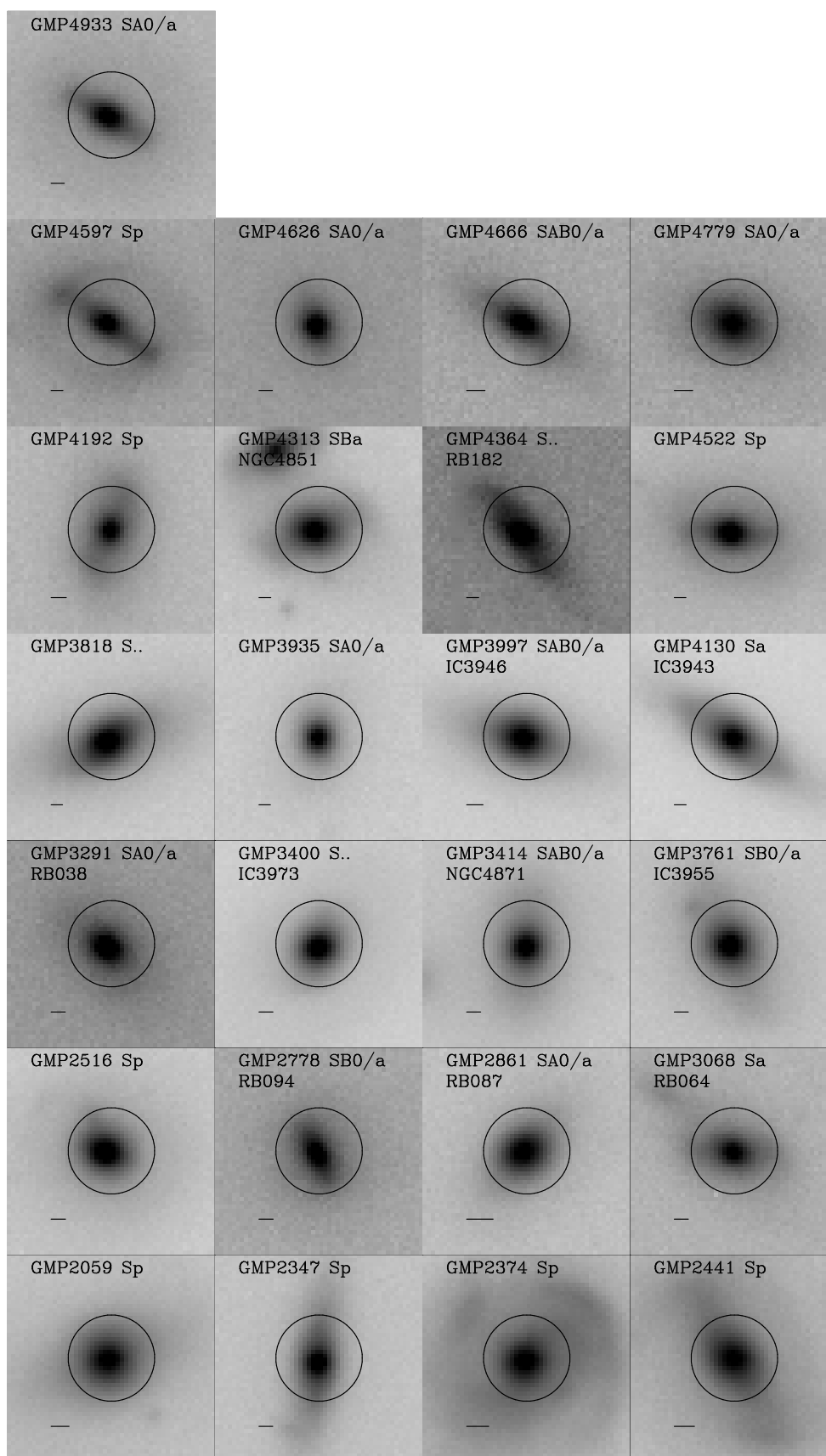


**Figure 8.** V band images of the late type galaxies which lie within  $3\sigma$  of the CMR for late type galaxies (dataset 7). The circle represents the  $13''$  diameter aperture used in the measurements of both the colours and the magnitudes for the results in table 6. The line in the lower left of each panel shows the width of the seeing disk in each image. The CMR for late types is identical to that of S0's, further strengthening the argument that these galaxies have mostly old stellar populations.

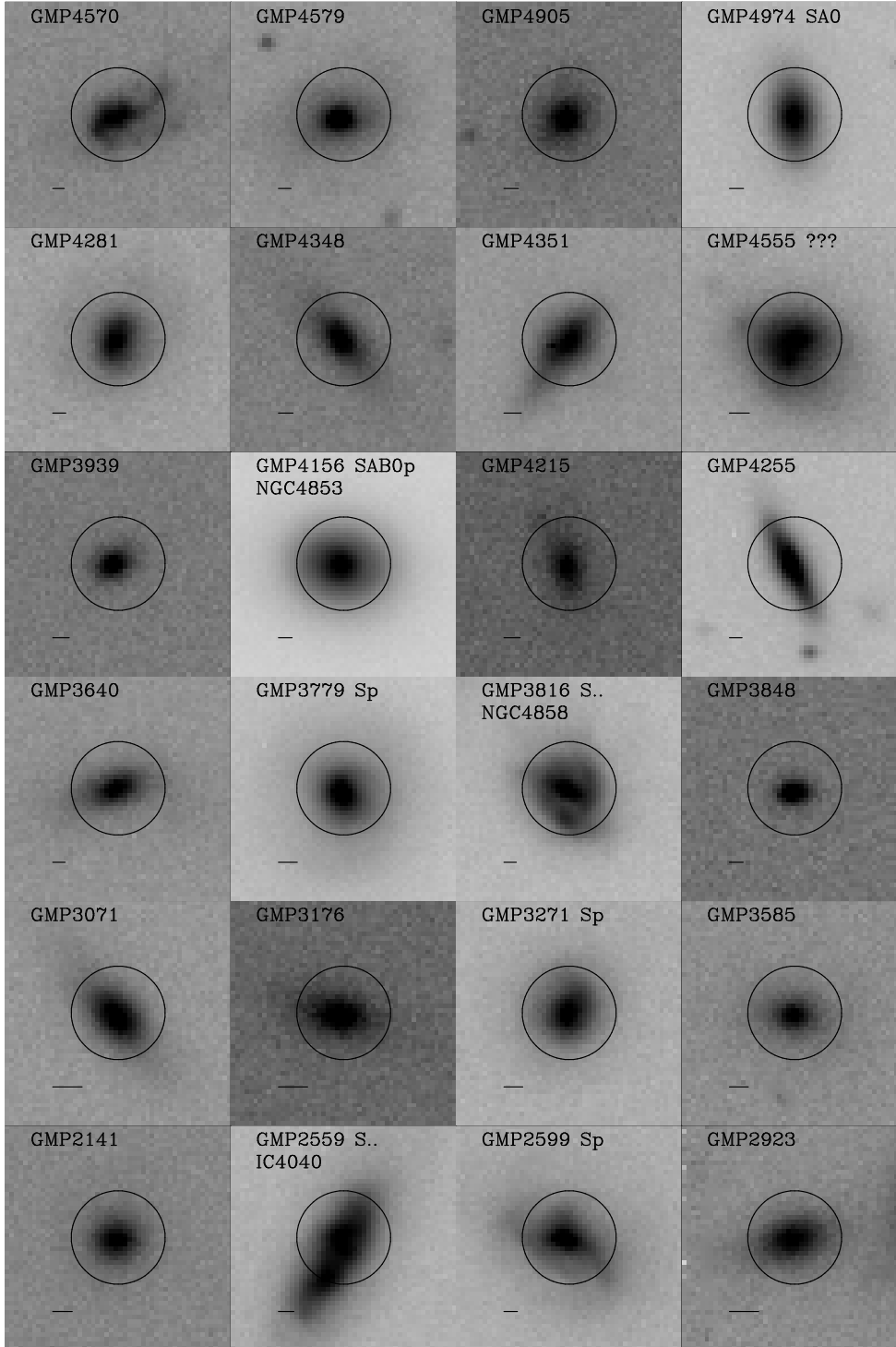


**Figure 9.** V band images of all of the galaxies which lie more than  $5\sigma$  blue-ward of the CMR for the members dataset (dataset 1). In addition to the galaxies identified as starburst or post-starburst in figure 5 (also present in this figure) GMP4255 (D44) is identified as a post-starburst and GMP4579 (D45) is identified as a starburst by Caldwell et al. (1993). Text and symbols in the plot are as for figure 8.

indistinguishable using both a K-S test, and a Student's  $t$  test (see section 5).

Another approach to analysing the environmental dependence of the CMR is to analyse the data by averaging over radial bins. Because there is insufficient data within a single bin, we use a running biweight to anal-

yse the radial dependence. We have excluded the galaxies around NGC4839 group in order to ensure that the radial sample also corresponds to a gradient in density. We ordered the galaxies according to their projected distance from NGC4874, and calculated running biweight location and scale indicators for the residuals from the CMR ridge

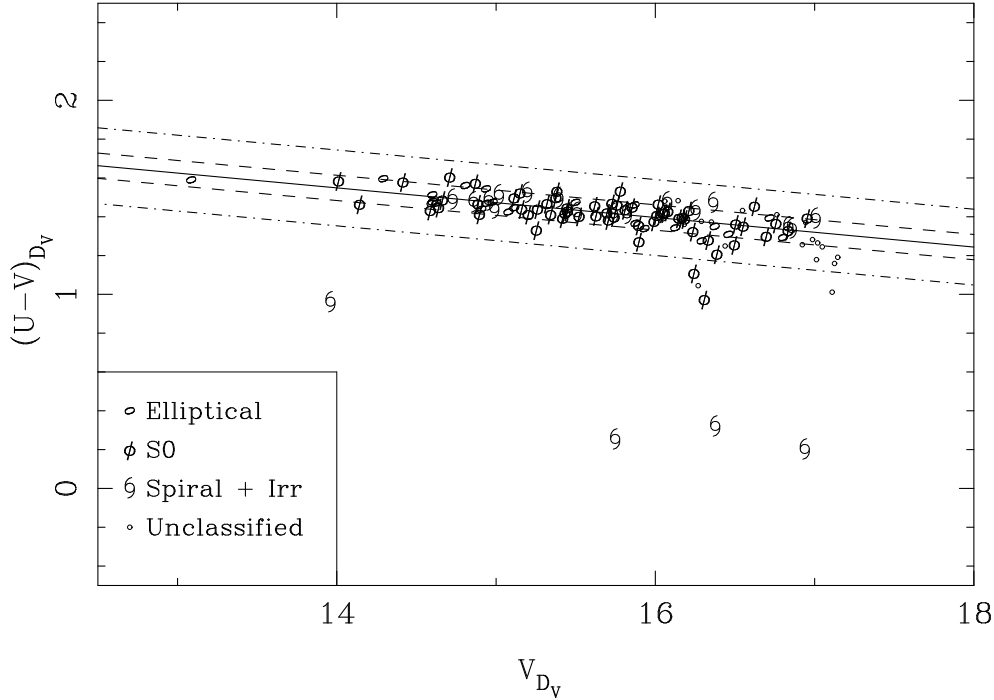


**Figure 10.** The colour-magnitude relation measured within the photometric diameter  $D_V$ . In this plot, the area within which the photometry is measured varies according to galaxy size.  $V_{D_V}$  is the V-band magnitude within the  $D_V$  diameter;  $(U - V)_{D_V}$  is the colour within this diameter.

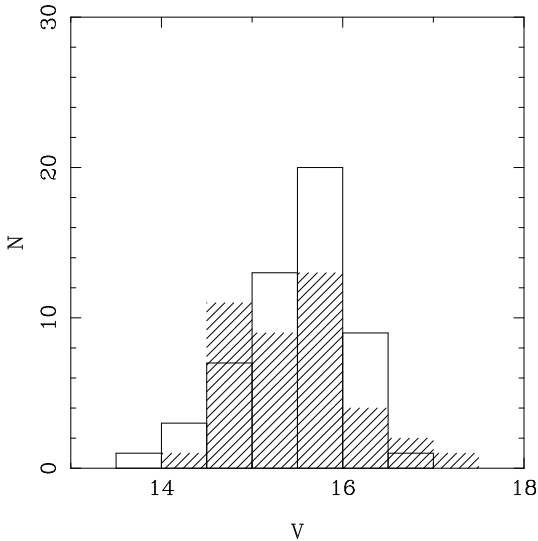


**Figure 11.** The luminosity distributions for the inner and outer E+S0 datasets (10 and 11). The lined histogram represents the luminosity distribution for the outer dataset (11) and the outlined histogram represents the luminosity distribution of the inner dataset (10). Both distributions are statistically indistinguishable using both a K-S test, and a Student's  $t$  test (see section 5)

line for three datasets, the full dataset (1), the early type galaxy dataset (4) and a dataset of just the S0 galaxies (5) (see figure 12). In all three panels, the  $(U - V)$  residuals are calculated using the best fit CMR to the whole data from table 6, such that negative values of  $\Delta(U - V)$  imply a galaxy is positioned to the blue side of the CMR ridge line. The first panel, using all the cluster members shows no in-

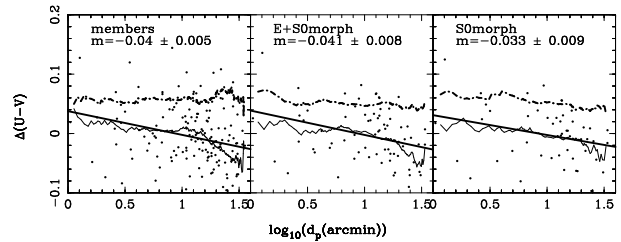


**Figure 12.** The residuals  $(U - V) - (mV + c)$  of each galaxy from the best fit CMR relation plotted against  $\log_{10}$  projected distance from NGC4874 in arc minutes for three of the datasets described in the text. Objects around NGC4839 have been excluded. The thin line shows the running biweight location indicator and the thick line shows the running scale indicator. Both indicators have a maximum binsize of 40. This reduces to 10 at both ends. The solid straight line is a biweight fit to all of the data, the slope of which ( $m$ ), and its  $1\sigma$  bootstrap error is shown in each panel.

crease in scatter with radius, however this could be affected by greater numbers of late type galaxies in the outer parts of the cluster. We therefore also show the colour residuals of the early type galaxy datasets (4 and 5). Again the scatter remains almost constant, with a very small downward gradient. All three panels show that the residuals from the CMR seem to be getting systematically bluer towards the edges of the cluster. It seems unlikely that this could be an age effect without also incurring an increase in the scatter of the CMR, which leaves two possibilities. Firstly it could simply be a radial drift in our photometric zero points. Although we checked for this against the data of BLE92a (see figure 3), it only extends out to a radius of 15 arc minutes, which is also where this effect begins to be noticeable. We

can however make a quick estimate of the expected drift in our photometry. We have on average 20 objects in the overlap regions, with RMS photometric errors of 0.026 mag (see table 2), which gives an RMS colour error between images of  $0.026/\sqrt{20}$ . Now to get to a radius of 30arcmin, we need to traverse at least 3 image boundaries, so the error accumulated is  $\sqrt{3} \times 0.026/\sqrt{20} = 0.01$  mag. However, the radius can be calculated in many different directions, and the photometric zero point for each image was indeed calculated in an iterative way such that any errors would dissipate in a two dimensional manner, so the value of 0.01mag (much smaller than the value of the colour gradient) can be regarded as an upper limit.

### 5.3.2 Dust

A possible explanation for the gradient could be that the galaxies in the center of the cluster are being reddened due to intracluster dust. The upper limit on the reddening through dust in the core of Coma, as compared to the field is  $E(U - V) \leq 0.08$  mag Ferguson (1993) could account for this amount of reddening, it could also add an extra source of scatter to the central parts of the cluster not present in the outer parts. Galaxies behind the cluster would appear both fainter and redder than an identical galaxy in front of the cluster. This would tend to increase the scatter in the CMR, but only in the central parts.

We can estimate the contribution of this dust to the scatter in the core of the cluster as follows. We define  $r$  as the distance from the core along the line of sight. If  $r_v$  is the virial radius of the cluster, then  $r = -r_v$  is the front of the cluster, and  $r = r_v$  is the rear of the cluster. We also assume that the galaxies and dust have the same isothermal density distribution, out to the virial radius:

$$\delta(r) = \begin{cases} \frac{1}{1 + \left(\frac{r}{r_c}\right)^2} & , \quad |r| \leq r_v \\ 0 & , \quad |r| > r_v \end{cases}$$

where  $r_c$  is the core radius. The amount by which a galaxy at  $r$  is reddened, is then

$$R(r) = \alpha r_c \left[ \arctan\left(\frac{r}{r_c}\right) + \arctan\left(\frac{r_v}{r_c}\right) \right]$$

$\alpha$  is a constant, which we chose in order to satisfy our boundary condition, that we get the required reddening in the center of the cluster, i.e.  $R(0) = 0.08$ mag (Ferguson 1993). We then calculate the mean and standard deviation of  $R(r)$ :

$$\bar{R} = \alpha r_c \arctan\left(\frac{r_v}{r_c}\right) = 0.08 \text{mag}$$

and

$$\bar{R}^2 = \frac{4}{3} \left( \alpha r_c \arctan\left[\frac{r_v}{r_c}\right] \right)^2 = \frac{4 \times 0.08}{3} \text{mag}^2$$

It should be noted that because of our choice of distributions for the dust and galaxies, both  $r_c$  and  $r_v$  have cancelled out of the calculations. The standard deviation of  $R(r)$  is then

$$SD(R) = \sqrt{\bar{R}^2 - \bar{R}^2} = 0.046 \text{mag}$$

It should be remembered that this is a very rough model for the distribution of dust and galaxies in the cluster. The distribution of dust especially is very poorly known. Clearly from the fact that the levels of scatter in this model is greater

that that measured for elliptical galaxies, we can say that the dust is either not distributed as an isothermal sphere, or that the limit for dust in the core is lower than the number quoted by Ferguson (1993).

### 5.3.3 Age

The other possibility for the bluing towards the edges, is a difference in mean galactic age. Using the models for a single burst stellar population of age 10Gyr from Bower et al. (1998), we find that  $d(U - V)/dt \sim 0.03$ mag/Gyr. This would make the outer galaxies approximately 2Gyr younger than the central galaxies. Assuming younger ages for the galaxy population would make the difference in age between the inside and the outside smaller, i.e. if the galaxies are only 5Gyr old, the difference in age between the inner and outer galaxies is only 1Gyr. Abraham et al. (1996) find a  $(g - r)$  colour gradient with projected radius in the  $z = 0.23$  cluster Abell 2390 of  $m = -0.08 \text{mag} \log_{10}(r_p)^{-1}$ , which they attribute to an age trend. To compare the Coma colour gradient with that of A2390, we used template early type galaxy spectra to K correct the Coma colours to the redshift of Abell 2390, and to convert them from  $U - V$  to  $g - r$ . We find that the gradient shown in figure 12 for early type galaxies, is transformed into  $m = -0.024 \text{mag} \log_{10}(r_p)^{-1}$ , a third of that measured in A2390.

A similar argument to the one above for the increased scatter in the core due to dust also applies in this case. When we look at the core, we also include galaxies in the foreground and background which are not in the cluster core, so are bluer than the core galaxies. This effect is not as large as the dust effect however, because the galaxies behind the cluster are just as blue as galaxies in front of it, so the effect is roughly half that expected from the dust model.

## 6 CONCLUSIONS

We have placed new limits on the levels of scatter in the  $(U, V)$  CMR of the Coma cluster. The cluster members were split into groups depending on their morphology, luminosity or position on the sky, and the CMR was studied in each of them. We found the properties of the ridge-line to be surprisingly consistent between all of these groups. We have also calculated upper and lower limits for the intrinsic scatter in each galaxy sample, taking into account the low number statistics that we are dealing with for some of them. The results are presented in tables 6-7.

We find no variation in the slope of the CMR ridge-line between Elliptical and S0 morphological types, The late type galaxies in the cluster have a marginally steeper slope. This could be connected to the increased blue scatter we find towards the faint end of the CMR. In the galaxies for which we have morphological types, all of these very blue galaxies are late types. All of the ‘blue’ galaxies, even where we don’t have morphological data, have colour gradients in the opposite direction to the normal CMR galaxies, i.e. the blue galaxies get redder with increasing galactic radius. This could be due to star formation constrained to the galaxy core and agrees with the findings of Moss & Whittle (2000), who show that a disturbed cluster galaxy morphology is a strong predictor of compact H $\alpha$  emission. Figure 9 shows

that even with our poor spatial resolution, which tends to make galaxies look of an earlier type, many of the unclassified blue galaxies are also of late type.

Although the bluest galaxies, tend to have late type morphology, there are many galaxies with late-type morphology whose colours are indistinguishable for E and S0 galaxies. The presence of such a large fraction of late-type galaxies on the CMR ridge line, with no increase in the CMR scatter, is surprising. However, figure 8 shows that our 13arcsec aperture is dominated by bulge light, and that in every case, the galaxies possess only a very faint disk. This could be a low redshift analogue of the trend seen in high redshift clusters by Dressler et al. (1997) who conclude that ellipticals predate the cluster virialisation, but that late type galaxies turn into S0 galaxies upon encountering the cluster. These anaemic spirals are likely to be galaxies in which star formation has been suppressed by ram-pressure stripping, but which still retain late-type characteristics (Poggianti et al., 1999).

Using the photometric diameter  $D_V$ , we have compared the colour magnitude relation found within a fixed 13'' diameter and that measured within  $D_V$ . As expected, that measured within  $D_V$  is shallower, due to colour gradients within the galaxies. The slope of the relation is still easily seen, however, showing that the intrinsic colours of galaxies vary systematically as a function of magnitude.

The slope of the CMR also remains constant as a function of radius within cluster, as expected from a universal metallicity–mass relation. We subtract the mean relation from the colours in order to study the gradients within the cluster. We find evidence for a gradient in the CMR corrected colours with projected cluster distance. Using a naive calculation for the expected slope in the photometric zero points, we conclude that it is at least a  $6\sigma$  result. The slope of the gradient is approximately one third the size of that found by Abraham et al. (1996) in the  $z = 0.23$  cluster Abell 2390, who attributed this to a gradient in the mean ages of the galaxies. We also find some evidence for decreasing scatter in the early type galaxies towards the outskirts of the cluster as compared with the central parts. The upper limit for  $E(U - V)$  (Ferguson 1993) in the cluster core is approximately equal to the  $U - V$  colour gradient observed, however we calculated the increased scatter produced in the CMR by the presence of enough dust in the cluster core to account for the colour gradient, and found that it was greater than the scatter observed in the elliptical galaxies. We therefore conclude that there cannot be sufficient dust in the cluster core to account for the entire gradient, and at least some of this gradient must be due to a systematic variation in galaxy age.

By comparing the colours with the stellar evolution models of Bower et al. (1998), we estimate that the maximum age difference between the galaxies in the center of the cluster, and in the outskirts is 2Gyr. Although younger galaxies show more scatter in the CMR than old galaxies (BLE92b; Bower et al. 1998), the core of the cluster is contaminated by young galaxies in front of and behind the cluster.

#### Acknowledgements

We thank John Lucey, Ian Smail and Jim Rose for help and useful discussions. We would also like to thank the referee

for many useful comments

This research has made use of the NASA/IPAC Extragalactic Database (NED) which is operated by the Jet Propulsion Laboratory, California Institute of Technology, under contract with the National Aeronautics and Space Administration.

#### REFERENCES

- Abraham R. G. et al., 1996, ApJ, 471, 694  
 Andreon S., Davoust E., Michard R., Nieto J. L., Poulain P., 1996, Astronomy and Astrophysics Supplement Series, 116, 429  
 Andreon S., Davoust E., Poulain P., 1997, Astronomy and Astrophysics Supplement Series, 126, 67  
 Arimoto N., Yoshii Y., 1987, A&A, 173, 23  
 Baier F. W., 1984, Astronomische Nachrichten, 305, 175  
 Beers T. C., Flynn K., Gebhardt K., 1990, AJ, 100, 32  
 Bender R., Burstein D., Faber S. M., 1992, ApJ, 399, 462  
 Bertin E., Arnouts S., 1996, Astronomy and Astrophysics Supplement Series, 117, 393  
 Bothum G. D., Dressler A., 1986, ApJ, 301, 57,  
 Bower R. G., Kodama T., Terlevich A. I., 1998, MNRAS, 299, 1193,  
 Bower R. G., Lucey J. R., Ellis R. S., 1992a, MNRAS, 254, 601  
 Bower R. G., Lucey J. R., Ellis R. S., 1992b, MNRAS, 254, 589  
 Caldwell N., Rose J. A., Franx M., Leonardi A. J., 1996, AJ, 111, 78  
 Caldwell N., Rose J. A., Sharples R. M., Ellis R. S., Bower R. G., 1993, AJ, 106, 473  
 Charlot S., Silk J., 1994, ApJ, 432, 453  
 Colless M., Dunn A. M., 1996, ApJ, 458, 435  
 Djorgovski S., Davis M., 1987, ApJ, 313, 59  
 Dressler A., 1980, ApJS, 42, 565  
 Dressler A., 1984, ApJ, 281, 512  
 Dressler A., Lynden-Bell D., Burstein D., Davies R. L., Faber S. M., Terlevich R., Wegner G., 1987, ApJ, 313, 42  
 Dressler A. et al., 1997, ApJ, 490, 577  
 Ellis R. S., Smail I., Dressler A., Couch W. J., Oemler J., A., Butcher H., Sharples R. M., 1997, ApJ, 483, 582  
 Escalera E., Slezak E., Mazure A., 1992, A&A, 264, 379  
 Faber S. M., 1973, ApJ, 179, 731  
 Ferguson H. C., 1993, MNRAS, 263, 343  
 Fried D. L., 1966, J. Opt. Soc. Am., 56, 1372  
 Frogel J. A., Persson S. E., Matthews K., Aaronson M., 1978, ApJ, 220, 75  
 Godwin J. G., Metcalfe N., Peach J. V., 1983, MNRAS, 202, 113  
 Johnson H. L., Morgan W. W., 1953, ApJ, 117, 313  
 Jorgensen I., Franx M., Kjaergaard P., 1993, ApJ, 411, 34  
 Kauffmann G., Charlot, S., 1998, MNRAS, 297, L23  
 Kodama T., 1997, Ph.D. thesis, Institute of Astronomy, University of Tokyo  
 Kodama T., Arimoto N., 1997, A&A, 320, 41  
 Kodama T., Arimoto N., Barger A. J., Arag'On-Salamanca A., 1998, A&A, 334, 99  
 Kodama, T., Bower, R. G., Bell, E. F., 1999, MNRAS, 306, 561  
 Kuntschner H., 1998, Ph.D. thesis, Department of Physics, University of Durham  
 Kuntschner H., Davies R. L., 1998, MNRAS, 295, L29  
 Landolt A. U., 1992, AJ, 104, 340  
 Larson R. B., 1974, MNRAS, 169, 229  
 Larson R. B., Tinsley B. M., Caldwell C. N., 1980, ApJ, 237, 692  
 Lucey J. R., Guzman R., , Carter D., Terlevich R. J., 1991, MNRAS, 253, 584  
 Maddox S. J., Efstathiou G., Sutherland W. J., 1990, MNRAS, 246, 433

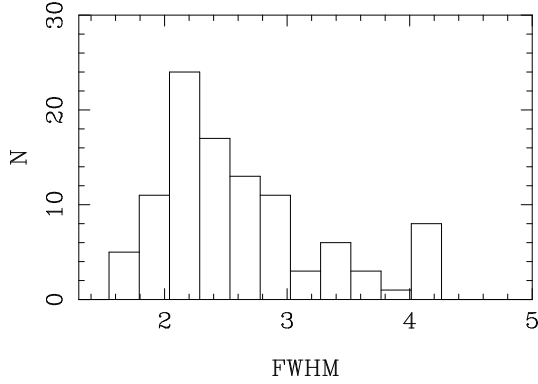


**Figure 13.** The distributions of the seeing FWHM obtained by least squares fitting of the profile of the brightest stars in each image to the theoretical seeing PSF described in equation 2.

- Mehlert D., Bender R., Saglia R. P., Wegner G., 1998, in *Untangling Coma Berenices: A New Vision of an Old Cluster*, p. 107
- Moss C., Whittle M., 2000, *MNRAS*, 317, 667
- Pahre M. A., Djorgovski S. G., De Carvalho R. R., 1995, *ApJ*, 453, L17
- Persson S. E., Frogel J. A., Aaronson M., 1979, *ApJS*, 39, 61
- Poggianti, B. M., Smail, I., Dressler, A., Couch, W. J., Barger, A. J., Butcher, H., Ellis, R. S., Oemler, A. J., 1999, *ApJ*, 518, 576
- Saglia R. P., Bender R., Dressler A., 1993, *A&A*, 279, 75
- Saglia R. P., Bertschinger E., Bagglely G., Burstein D., Colless M., Davies R. L., McMahan J., R. K., Wegner G., 1993, *MNRAS*, 264, 961
- Secker J., Harris W. E., Plummer J. D., 1997, *PASP*, 109, 1377
- Stanford S. A., Eisenhardt P. R., Dickinson M., 1998, *ApJ*, 492, 461
- Terlevich, A. I., Kuntschner, H., Bower, R. G., Caldwell, N., Sharples, R. M., 1999, *MNRAS*, 310, 445
- Vader J. P., 1986, *ApJ*, 306, 390
- Van Den Bergh S., 1991, *PASP*, 103, 390
- Visvanathan N., Sandage A., 1977, *ApJ*, 216, 214
- Woolf N. J., 1982, *ARA&A*, 20, 367
- Worthey G., 1994, *ApJS*, 95, 107
- Zepf S. E., Whitmore B. C., Levison H. F., 1991, *ApJ*, 383, 524

## APPENDIX A. SEEING CORRECTIONS

In this discussion, we restrict ourselves to a circularly symmetric PSF. All our measured properties are circularly averaged, so any non spherical symmetry in the PSF, due maybe to poor tracking or focus, would cause only second order effects (Saglia et al. 1993).

The Fourier transform of the PSF can be predicted using atmospheric turbulence theory to be  $\exp[-(kb)^{5/3}]$  (Fried 1966; Woolf 1982), where the scaling parameter  $b = FWHM/2.9207006$ . We generalise this to

$$\hat{p}_\gamma(k) = \exp[-(kb)^\gamma] \quad (2)$$

where  $\gamma$  controls the amount of light in the wings of the PSF.  $\gamma = 2$  corresponds to a Gaussian profile, while the theoretically predicted value of  $\gamma = 5/3$  gives a more wingy PSF. Lower values of  $\gamma$  produce even larger wings (e.g. Saglia et al., 1993).

We used least square fits of the brightest stellar objects

in each image to obtain both  $\gamma$  and  $b$  for each exposure. Figure 13 shows the distribution of FWHM for all of our images. Although the values of  $\gamma$  vary from 1.2 to 1.8 (although mainly clustered around 1.45), there is very little variation between stars in the same exposure, so when calculating the final seeing correction for a galaxy, we use the  $\gamma$  corresponding to the image the galaxy was measured from

The Intensity at a radius  $R$  from a source ( $I(R)$ ), is then given by the convolution of the surface brightness distribution of the object in the sky ( $I^s(R)$ ) with the PSF ( $p_\gamma(R)$ ).

$$I(R) = I^s(R) \otimes p_\gamma(R) \quad (3)$$

For stellar objects, we simply take the intensity distribution on the sky to be a delta function, and for galaxies, we use the canonical deVaucouleurs  $R^{1/4}$  law.

$$I^s(R) = \begin{cases} I_e \exp\left\{-7.669 \left[\left(\frac{R}{R_e}\right)^{1/4} - 1\right]\right\} & , \text{ galaxy} \\ L\delta_D(R) & , \text{ star} \end{cases}$$

where  $R_e$  is the half light radius, at which  $F(R_e) = F(\infty)/2$ ,  $I_e = I(R_e)$ ,  $\delta_D(R)$  is the Dirac delta and  $L$  is the luminosity of the star.

To convert the luminosity distributions of an object in the sky into the luminosity distribution of the object on the detector we must convolve with the PSF (equation 3).

To seeing correct our objects we require the difference, in magnitudes, of the flux of an object as measured within an aperture of radius  $R$  on our detector ( $F(R)$ ), and its flux as measured within the same aperture on the sky ( $F^s(R)$ ). To find the flux inside an aperture of radius  $R$ , we simply integrate the required luminosity distribution,

We found the value of  $R_e$  to gave little effect on the seeing correction, for all  $R_e \leq 1$  so we use  $R_e = 5''$  for all of our galaxies.

Numerical integration techniques were used to perform both the integrations and the convolutions. The results of which, for a variety of apertures and seeing FWHM are shown in tables 8 and 9. Both of these tables assume  $\gamma = 1.47$ , the average value for our observations.

## APPENDIX B. PHOTOMETRIC CALIBRATION VIA FRAME OFFSETS

The method we used to generate this system is very similar to that used in Maddox et al. (1990) to homogenise the APM galaxy catalogue. However, it is far simpler due to our detector's better flat fielding and its linearity.

To calculate a set of zero-point offsets for each image the regions of overlap between each pair of images was examined. An object positioned in an area where frames  $i$  and  $j$  overlap will have magnitudes  $m_i$  and  $m_j$  as measured from frames  $i$  and  $j$  respectively. The actual magnitude for this object is  $m_0$ , and in the absence of observational errors, these three quantities can be related to each other thus,

$$m_0 = m_i + C_i = m_j + C_j \quad (4)$$

where  $C_i$  is the correction applied to the zero point of image  $i$ . If we define

$$T_{ij} = m_i - m_j = C_j - C_i$$

as the overlap difference between  $i$  and  $j$ , then the offset

**Table 8.** Table of galaxy seeing corrections based on a galaxy with  $R_e = 5$ arcsec. To obtain the seeing corrected value, the seeing correction is subtracted from the observed aperture magnitude. We parameterise the profile of the PSF using  $\gamma = 1.47$ , the average  $\gamma$  for our observations. Corrections are show for circular apertures ranging from 4 to 60arcsec diameters. When seeing correcting our data, we calculated a correction for each image by fitting a FWHM and  $\gamma$  to it from the bright stars.

seeing FWHM	Aperture diameter (arcsec)											
	4	6	8	10	13	16	20	25	32	40	50	60
4.50	0.909	0.564	0.376	0.268	0.176	0.126	0.087	0.060	0.039	0.027	0.018	0.014
4.00	0.789	0.476	0.314	0.222	0.146	0.104	0.072	0.050	0.033	0.022	0.015	0.011
3.50	0.667	0.391	0.254	0.180	0.118	0.085	0.059	0.041	0.027	0.018	0.012	0.009
3.00	0.542	0.309	0.200	0.141	0.093	0.067	0.046	0.032	0.021	0.014	0.010	0.007
2.50	0.418	0.233	0.150	0.106	0.070	0.050	0.035	0.024	0.016	0.011	0.007	0.005
2.00	0.300	0.165	0.106	0.075	0.050	0.036	0.025	0.017	0.011	0.008	0.005	0.004
1.50	0.193	0.106	0.068	0.049	0.032	0.023	0.016	0.011	0.007	0.005	0.003	0.002
1.00	0.104	0.057	0.037	0.027	0.018	0.013	0.009	0.006	0.004	0.002	0.001	0.001

**Table 9.** Table of stellar seeing corrections. To obtain the seeing corrected value, the seeing correction are subtracted from the observed aperture magnitude. We parameterise the profile of the PSF using  $\gamma = 1.47$ , the average  $\gamma$  for our observations. Corrections are show for circular apertures ranging from 4 to 60arcsec diameters. When seeing correcting our data, we calculated a correction for each image by fitting a FWHM and  $\gamma$  to it from the bright stars.

seeing FWHM	Aperture diameter (arcsec)											
	4	6	8	10	13	16	20	25	32	40	50	60
4.50	1.093	0.573	0.332	0.214	0.129	0.088	0.060	0.041	0.028	0.020	0.014	0.011
4.00	0.922	0.461	0.263	0.170	0.104	0.072	0.049	0.034	0.023	0.016	0.012	0.009
3.50	0.746	0.357	0.202	0.132	0.082	0.057	0.040	0.028	0.019	0.013	0.010	0.007
3.00	0.573	0.263	0.150	0.099	0.063	0.044	0.031	0.022	0.015	0.011	0.008	0.006
2.50	0.408	0.184	0.107	0.072	0.046	0.033	0.023	0.016	0.011	0.008	0.006	0.004
2.00	0.263	0.120	0.072	0.049	0.032	0.023	0.016	0.012	0.008	0.006	0.004	0.003
1.50	0.150	0.072	0.044	0.031	0.020	0.015	0.011	0.008	0.005	0.004	0.003	0.002
1.00	0.072	0.037	0.023	0.016	0.011	0.008	0.006	0.004	0.003	0.002	0.001	0.001

correction for any image can be calculated from the overlap differences and offset corrections of any adjacent overlapping image.

$$C_{ij} = C_j + T_{ij}, \forall j \subset i$$

where  $j \subset i$  denotes any pair of images  $i, j$  with a valid overlap region, and  $C_{ij}$  denotes the  $C_i$  as calculated from image  $j$ . Firstly we construct an observed estimate of the  $T_{ij}$ .

$$T_{ij}^e = \frac{\sum_{n=1..N_{ij}} (m_{n_i} - m_{n_j})}{N_{ij}}$$

where  $N_{ij}$  is the number of bright objects in the region of overlap between images  $i$  and  $j$ , and the  $m_{n_i}$  and  $m_{n_j}$  are the measured magnitudes of object  $n$  in images  $i$  and  $j$  respectively.

Now we can use a weighted mean of the  $T_{ij}^e$  to find a value for the photometric offsets.

$$C_i^{n+1} = \frac{\left( C_i^n W_i + \sum_{j \subset i} (C_j^n + T_{ij}^e) W_{ij} \right)}{\left( W_i + \sum_{j \subset i} W_{ij} \right)} \quad (5)$$

where the  $C_i^n$  are the  $C_i$  calculated in iteration  $n$ ,  $W_i$  is the mean of the weights,  $W_{ij}$ . These weights were chosen to be proportional to the number of objects used to calculate the  $T_{ij}^e$ , and normalised to be in the range zero to one. We chose to use the number in the overlap ( $N_{ij}$ ), rather than

the inverse of the scatter in the  $(m_{n_i} - m_{n_j})$ . With the low number of objects present in our overlaps, the scatter is not always well determined, and can be artificially low for overlaps with low  $N_{ij}$ , just the opposite of the required behaviour.

This iterative method does not constrain the total photometric offset, it merely ensures the best possible relative photometry of the system by removing as much of the drift in the zero point between images as is possible in a self consistent manner. We therefore arbitrarily re-normalise the  $C_i$  after every iteration so that they have zero mean.

Equation 5 was iterated to find the best set of  $C_i$ . To measure the progress of the iterations, we construct a measure of the homogeneity of the system after iteration  $n$ ,

$$E^n = \sum_{i=1..N} \sum_{j \subset i} W_{ij} (T_{ij} + C_i^n - C_j^n)^2 \quad (6)$$

where  $N$  is the total number of images for which we are trying to ascertain the  $C_i$ s. We iterate until the rate of change of  $E^n$  has slowed to less than  $E^n/1000$  per iteration.

Obviously much care has to be taken in the measurement of the  $T_{ij}^e$ . We must ensure that effects such as different seeing conditions on the two overlapping images do not cause any systematic offsets. Although seeing conditions are taken into account for each object when measuring the  $m_i$  (see section 6), the effect of seeing on objects adjacent to the aperture are not corrected for i.e. more light from an adjacent object will enter the aperture for images with worse seeing. We therefore measured the  $m_i$  in various sized apertures, from 8.8'' to 26'' diameter, and using background

annuli from 20'' to 100'' diameter with 25'' and 3.2'' widths. If the  $T_{ij}$  are well behaved under all measuring conditions, then we simply take the median value. If they are not well behaved, we inspect the region more carefully to ascertain the cause, or we mark the  $T_{ij}$  as unreliable.

To summarise, we can now construct a homogeneous dataset by adding to each magnitude  $m_i$ , the offset correction for the image in which it was measured ( $C_i$ ) to obtain the object's corrected magnitude  $m_0$  (see equation 4). This homogeneous photometric system however is only relative. To set the overall photometric offset, we use the fixed aperture magnitudes of BLE92a. We have new observations of all of the BLE92a sample, so using these galaxies we can define a transformation between our corrected aperture magnitudes, and theirs. We conclude that our V band response is similar to that of BLE92a, but the larger value of the U-band colour term indicates that our U band response is not such a good match, probably due to our increased sensitivity to the blue portion of the U bandpass.